Journal of Alloys and Compounds 509 (2011) 4999–5007

Contents lists available at ScienceDirect

Journal of Alloys and Compounds

journal homepage: www.elsevier.com/locate/jallcom

One-step synthesis and properties of monolithic photoluminescent ruby colored cuprous oxide antimony oxide glass nanocomposites

Tirtha Som, Basudeb Karmakar*

Glass Science and Technology Section, Glass Division, Central Glass and Ceramic Research Institute, Council of Scientific and Industrial Research (CSIR, India), 196, Raja S.C. Mullick Road, Kolkata 700032, India

ARTICLE INFO

Article history:
Received 8 April 2010
Received in revised form 27 January 2011
Accepted 31 January 2011
Available online 27 February 2011

Keywords:
Nanostructured materials
Optical materials
Optical properties
Luminescence

ABSTRACT

Cuprous oxide (Cu_2O) antimony glass (K_2O–B_2O_3–Sb_2O_3) monolithic nanocomposites having brilliant yellow to ruby red color have been synthesized by a single-step melt-quench technique involving in situ thermochemical reduction of Cu^{2+} (CuO) by the reducing glass matrix without using any external reducing agent. The X-ray diffraction (XRD), infrared transmission and reflection spectra, and selected area electron diffraction analysis support the reduction of Cu^{2+} to Cu^{+} with the formation of Cu_2O nanoclusters along with $Cu_ySb_{2-x}(O,OH)_{6-7}$ ($y \leq 2$, $x \leq 1$) nanocrystalline phases while Cu^0 nanoclusters are formed at very high Cu concentration. The UV–vis spectra of the yellow and orange colored nanocomposites show size-controlled band gap shift of the semiconductor (Cu_2O) nanocrystallites embedded in the glasses while the red nanocomposite exhibits surface plasmon resonance band at 529 nm due to metallic Cu. Transmission electron microscopic image advocates the formation of nanocystallites (5–42 nm). Photoluminescence emission studies show broad red emission band around 626 nm under various excitation wavelengths from 210 to 270 nm.

1. Introduction

Productions of colored (or "striking") glasses by incorporating semiconductors (like colloidal particles of Cu_2O, CdS, CdSe, CdTe, $CdSSe_x$, etc.) or metal nanoclusters (like Cu, Au, Ag) have a very interesting history [1–4]. Both the copper- and gold-ruby glasses, in particular, have captured sustained interest of mankind since the Roman times due to their distinctive red color and their fabrication and investigation of the origin of red color still continue to be an interesting branch of glass research [5–9]. Although Au and Cu rubies had initially received significant importance for their applications as decorative items and red filter glasses, but with the introduction of selenium based ruby glasses [10], their commercial importance as filter glass started to diminish gradually. This is mainly because the ruby glasses based on the $CdSSe_x$ (semiconductors) have steep absorption edges in the visible region corresponding to saturated colors where in the case of gold (metallic) ruby glasses the tail of the transmission edges often reaches far into the short-wavelength region thereby producing a blue tint in the red color [2]. It is interesting to note that costly selenium ruby glass is produced in appreciable quantity in the Indian subcontinent and south-east Asia by a special branch of the glass industry, namely the glass bangle industry which is one of the biggest cottage industries in these countries. Since the ores of selenium in these regions is scarce, there is often scarcity of this material. Consequently, synthesis of ruby red glasses by involving simple processes and cheap resources deserve considerable attention.

The electronic configuration of copper enables it to exist in different oxidation states in glasses like Cu^{2+}, Cu^{+} and Cu^0 and even as Cu_2O nanocrystals. Each of these species imparts a distinct color to the host glass depending on their coordination geometry and electronic transitions between their exclusive energy levels. So the thermodynamic activity of cuprous–cupric redox reaction in glasses has been subjects of several investigations [11,12]. The incorporated copper in various oxidation states not only influences structural properties, but spectroscopic and electrical properties as well [13–16]. It is known that introduction of copper oxide (CuO) in glass batch imparts red color under reducing conditions (in presence of $SnCl_4$, SnO_2, Sb_2O_3) of melting [17–19] but its production particularly in regard to brightness and uniformity of color has been reported to be the most difficult one [1,2].

The origin of a red color in case of Cu-ruby glasses has been attributed either to the presence of both copper clusters and cuprous oxide or solely to copper nanoparticles [5–8]. Initially, it was suggested that the origin of color in Cu rubies was due to precipitation of fine metallic Cu [1,20]. Later, this was supported by optical absorption spectroscopy and electron microscopy which

* Corresponding author. Tel.: +91 33 2473 3469; fax: +91 33 2473 0957.
E-mail address: basudebk@cgcri.res.in (B. Karmakar).

0925-8388/$ – see front matter © 2011 Elsevier B.V. All rights reserved.
doi:10.1016/j.jallcom.2011.01.208

emphasized plasmonic Cu nanoparticles (NPs) give rise to surface plasmon resonance (SPR) absorption band at around 570 nm [21]. The absorption band in this region is responsible for the color on copper-ruby glasses. Secondly, Ram and Prasad [22] have reported that the absorption band at 570 nm also can be explained by colloidal Cu_2O particles and this idea has been supported by both thermodynamic calculation [11] but by electron spectroscopy for chemical analysis (ESCA) measurements as well [23]. Although Cu^+ ion ($3d^{10}$) is not expected to produce coloration in glass due to lack of $d \rightarrow d$ electron transition. However, it has been demonstrated that, under special conditions (reducing atmosphere), the Cu(I) ion can be precipitated as colloidal particles of Cu_2O, which then would be responsible for the ruby color [22]. This is because Cu_2O is a semiconductor, and its band gap energy is about 2.17 eV, which is considered to be the origin of the red color of Cu_2O [5,24]. It may be interesting to note that the mineral cuprite, Cu_2O, has a bright ruby color. Later on, based on several characterization techniques Nakai et al. [5], Brun et al. [25] and Fernandez-Navarro et al. [26] have suggested that both Cu as well as Cu_2O nanoparticles participate in the coloring mechanism of ruby glasses.

Emission and other properties of Cu^0 as well as Cu_2O nanocrystals have been studied in solution by several researchers [27–30]. Cu_2O in particular have revealed distinctive optical, photoelectrical, electrical, physical and photocatalytic properties among the numerous transition metal semiconducting oxides [31,32]. But the introduction of Cu_2O or Cu nanoparticles into conventional glass matrices (like silicate, borate, phosphate, etc.) are usually achieved by intricate multistep procedures like sol–gel techniques, ion-exchange of the thin glass plates followed by X-ray, ion-beam or laser irradiations and ion-implantation and ion-exchange followed by heat treatment in reducing (hydrogen) atmosphere, sputtering techniques [19,21,33–41]. Sol–gel techniques have been specially adopted by De et al. [35] to synthesize monolithic ruby glasses. Bring et al. [19] investigated the effect of minor additions of Sb^{3+} and Sn^{2+} during the heat treatment of copper ruby alkali silicate glasses. Gil et al. [36,37] obtained both yellow and red superficially colored Ag-doped lead glasses by doping minor amounts of reducing agent like Sb_2O_3, As_2O_3, SnO_2 and CeO_2 to Ag^+ ion-exchanged glasses to facilitate reduction of Ag^+ to Ag^0 and taking advantage of red-shift of the plasmon band of Ag in high refractive index lead glasses. Efforts have been made by Capatina [38] to obtain Cd (another highly toxic element) free ruby red glasses by reducing Cu with Sn.

To the best of our knowledge, antimony (III) oxide (Sb_2O_3) has only been incorporated in minute quantities in batches of other glasses to serve as a reducing/fining agent, the incorporation of Cu_2O and Cu nanoparticles in antimony glass matrix and its property evaluation have not reported previously. In fact, the area of nano metal-doped and semiconductor doped Sb_2O_3 based glasses and nanocomposites have remained totally unexploited because of their difficulties in preparation particularly in the monolithic form which is very much essential for practical applications. The difficulties arises because Sb_2O_3 is an intermediate category of glass forming oxide, does not readily form glass [2,41]. Earlier reports on synthesis of antimony glasses show that they are obtained only as tiny pieces [2,42]. However, the excellent optical, dielectric, and particularly chemical (mildly reducing) properties render them as excellent choices for the development of advanced nanocomposites.

The aim of the present paper is to obtain bulk (monolithic) antimony glass-based nanocomposite having brilliant, permanent and homogeneous ruby red color by a single-step melting process, by the formation and homogeneous dispersion of nanosized cuprous oxide involving the reduction of copper oxide within a reducing antimony glass (K_2O–B_2O_3–Sb_2O_3) matrix without the addition of any other external reducing agent. However such thermochemical process is also found to be accompanied by the formation of Cu NPs and mixed crystals of copper antimony oxides ($Cu_ySb_{2-x}(O,OH)_{6-7}$) ($y \leq 2$, $x \leq 1$). All the resultant nanocomposites have been characterized by X-ray diffraction (XRD), energy-dispersive X-ray (EDX), UV-Vis-NIR absorption and transmission, transmission electron microscopy (TEM), selected-area electron-diffraction (SAED) analysis, the infrared transmission (FT-IRTS), and infrared reflection (FT-IRRS) spectroscopies. Their photoluminescence properties have also been evaluated.

2. Experimental details

2.1. Raw materials

The raw materials were potassium metaborate, $KBO_2 \cdot xH_2O$ (15.7% H_2O) of Johnson Matthey, antimony (III) oxide, Sb_2O_3 (GR, 99%) of Loba Chemie and copper (II) oxide, CuO (AR, 99%) of s.d. fine-Chem. They were used directly without any further purification.

2.2. Synthesis of nanocomposites

The base glass (G) has composition $15K_2O$–$15B_2O_3$–$70Sb_2O_3$ (mol%). Approximately 20 g base glass batch was mixed with required weighed amount of the components and melted in a high purity silica crucible at 900 °C for 10 min under ambient atmosphere. The batch filled crucible was placed directly at the hearth of the melting furnace previously raised to 900 °C temperature. Unlike the melting schedules usually followed for conventional glasses, here the melting time has to be kept small to prevent high vaporization rate of Sb_2O_3 and within this optimum time, the reactants also undergo complete reaction. The molten glass is stirred with a high purity silica rod for about 0.5 min to attain near-complete homogeneity, cast on carbon plates, annealed at 260 °C for 3 h to relieve the internal stress and then very slowly cooled to room temperature at the rate of 1 °C/min.

All the nanocomposites (NC1–NC8) were prepared in the similar simple technique just by adding the required quantity of dopant CuO (concentration in excess and in terms of wt% of Cu) to the batch composition of the base glass. Here it must be emphasized that the synthesis of the nanocomposites requires no other special techniques (like long term heat treatment, etc.) to be adopted. Samples of about 1.0 ± 0.01 mm thickness were polished for optical measurements.

2.3. Characterization of nanocomposites

The density of the glass and nanocomposites were measured by Archimedes method using toluene as the immersion liquid with an accuracy of ±0.7%. To confirm the existence of Cu in the nanocomposites, qualitative elemental composition analysis was performed using energy-dispersive X-ray spectroscopy. The XRD patterns of the bulk samples were recorded in an X'pert Pro MPD diffractometer (PANalytical) operating at 40 kV and 30 mA using Ni-filtered CuKα radiation with the X'celerator with step size 0.05° (2θ) step time 0.5 s, from 10° to 80°. The UV-Vis-NIR absorption and transmission spectra in the range 300–1100 nm were recorded with a double-beam spectrophotometer (PerkinElmer, Lambda 20) at the accuracy of ±0.1 nm. TEM measurements were carried out with a JEOL 2010 microscope and SAED analysis of the nanoparticles was also performed. The FT-IRTS of the raw materials, base glass and nanocomposites in the range 4000–400 cm^{-1} were recorded by following the KBr pellet method with a Fourier transform infrared (FTIR) spectrometer (PerkinElmer, FTIR 1615) at a resolution of ±2 cm^{-1} and after 16 scans to identify the bond vibrations (absorption peaks) particularly in the fingerprint region. The FT-IRRS in the range 400–1500 cm^{-1} were recorded with the same instrument at an incident angle of 15° and with the help of a specular reflectance attachment accessory at the resolution of ±1 cm^{-1} and after 256 scans. Fluorescence spectra were measured, at the accuracy of ±0.2 nm, with a fluorescence spectrophotometer (Spex, Fluorolog 2) with Xenon lamp as excitation source and a photomultiplier tube as a detector. All the measurements were carried out at room temperature.

3. Results and discussion

3.1. Physical properties

Composition of the base glass and nanocomposites (NC1–NC8) and some of their properties (observed, measured and calculated) are listed in Table 1. All nanocomposites are obtained in monolithic form except NC8. The base glass had a very faint yellow coloration caused by transition between HOMO (Sb 5s + O 2pπ) and LUMO (Sb 5p) [41].

The densities of the nanocomposites are found to increase with increase in Cu concentration. All the doped nanocomposites show

Table 1
Composition and some physical properties of base glass and nanocomposites.

Glass/composite identity	Concentration of Cu (wt%)	Color of composite	Nature of composite obtained	Density, ρ (g cm^{-3})	Band gap, E_g (eV)	Calculated average mixed crystallite diameter at $2\theta = 30.169^\circ$ from Eq. (1) (±1, nm)
G[a]	0	Pale yellow	Monolith	4.5560	3.33	
NC1	0.20	Yellow	Monolith	4.5582		
NC2	0.50	Yellow	Monolith	4.5634	3.12	
NC3	1.00	Yellow	Monolith	4.5775	2.78	
NC4	1.50	Deep yellow	Monolith	4.5962	2.67	
NC5	2.00	Deep yellow	Monolith	4.6136	2.63	35
NC6	2.50	Orange	Monolith	4.6176	2.47	40
NC7	3.00	Ruby red	Monolith	4.6181	2.16	47
NC8	3.50	Deep red	Broken pieces			70

[a] Base glass (G) composition (mol%): $15K_2O$–$15B_2O_3$–$70Sb_2O_3$.

uniform bright coloration which changes from yellow to orange to red (Table 1 and Fig. 1) due to quantum size effects [30,35,43]. Smaller QDs of Cu_2O exhibit yellow coloration which gradually transforms into brilliant red coloration as bulk size is approached. Similar observations have been recorded for CdS and PbS (CdS QDs are white while bulk CdS is orange; PbS QDs are yellow-brown while bulk PbS is black) [43]. Ahmed and Ashour [44] reported that in Cu_2O aventurine glass, the precipitated Cu_2O in the aventurine glasses exhibits different colors ranging from yellow to red depending on the synthetic conditions and on the heat-treatment temperature. Their electron microscopic study has exposed that when the Cu_2O crystals have diameters <5 μm, they are yellow, and when their diameter is >150 μm they are red, whereas crystals with diameters falling between this range are orange.

The chemical compositions of all the nanocomposites (NC1–NC8) were examined using energy-dispersive X-ray spectroscopy and they confirmed the presence of copper in the antimony matrix. A representative EDX spectrum of nanocomposite NC5 is shown in Fig. 2. EDX spectrum also shows negligible silica contamination from silica crucible.

3.2. XRD crystallographic analysis

Fig. 3 clearly represents the XRD pattern of synthesized NCs, NC4–NC8. The nanocomposites NC1–NC3 did not show any distinct peaks in the XDR spectra possibly due to very small concentration of nanocrystallites to appear in the XRD. So, their XRD patterns have not been represented. The broad XRD bands between 25° and 35° indicate amorphous nature of the synthesized NCs due to the presence of uncrystallized residual antimony glass. For curves b–e, the sharp peak at $2\theta = 30.1699^\circ$ ($d = 2.96288$ Å) growing together with the second reflection at $2\theta = 15.0631^\circ$ ($d = 5.88179$ Å) suggests the formation of mixed copper antimony oxides ($Cu_ySb_{2-x}(O,OH)_{6-7}$)

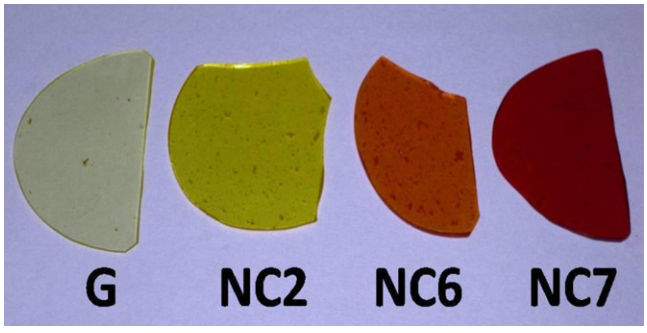

Fig. 1. Photograph showing the change of color of glass and nanocomposites with Cu concentration (for composition see Table 1).

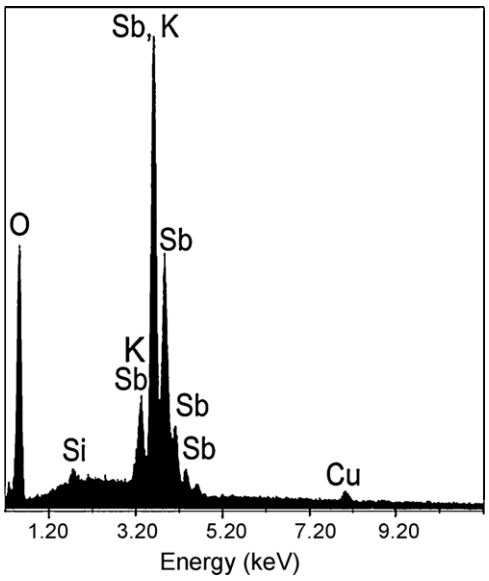

Fig. 2. EDX spectrum of a nanocomposite particle in composite NC5 (for composition see Table 1).

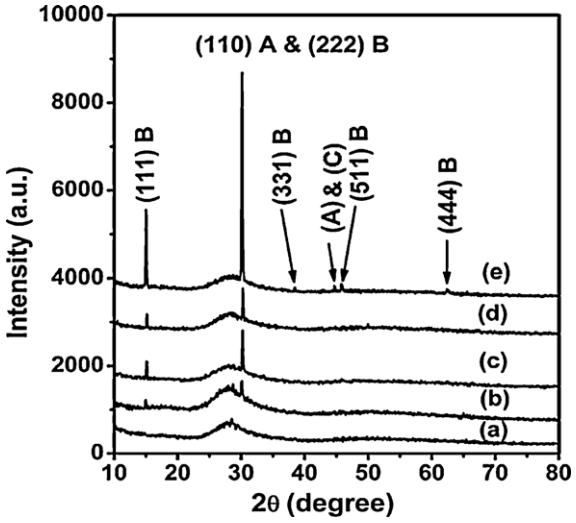

Fig. 3. X-ray diffractograms of nanocomposite: (a) NC4, (b) NC5, (c) NC6, (d) NC7 and (e) NC8 (for composition see Table 1), where A = Cu_2O, B = $Cu_ySb_{2-x}(O, OH)_{6-7}$ ($y \leq 2, x \leq 1$) and C = Cu (please note that $2\theta = 44.7645^\circ$ ($d = 2.02460$ Å) indicates both Cu and Cu_2O crystals but no ($h\,k\,l$) value of Cu_2O is provided in its JCPDS card file no. 35-1091).

($y \leq 2$, $x \leq 1$) (JCPDS card file no. 7-0303) and corresponds to its (2 2 2) and (1 1 1) planes diffractions respectively. Again the small peaks at $2\theta = 38.4497^\circ$ ($d = 2.34131$ Å), 45.8144° ($d = 1.98062$ Å) and 62.4378° ($d = 1.48741$ Å) corresponds to (3 3 1), (5 1 1) and (4 4 4) diffractions from $Cu_ySb_{2-x}(O,OH)_{6-7}$ crystals, thereby emphasizing its presence. It should also be noted that very high intensity peak at $2\theta = 30.1699^\circ$ coincides with (1 1 0) diffractions of Cu_2O (JCPDS card file no. 34-1354). The ratio of the peaks at 15.0631° and 30.1699° should be 1:1.1 in case of $Cu_ySb_{2-x}(O,OH)_{6-7}$ ($y \leq 2$, $x \leq 1$) crystals but practically the observed ratio is 1:2.5. This also emphasizes the probable presence of Cu_2O crystals. Again, the small peak at $2\theta = 44.7645^\circ$ ($d = 2.02460$ Å) also suggests the presence of Cu_2O crystals (JCPDS card file no. 35-1091) and thereby supports the in situ reduction of Cu^{2+} (CuO) to Cu^+ (Cu_2O) by Sb_2O_3. Interestingly, the d-value of this peak at 44.7645° also agree with that of the (1 1 1) plane of Cu nanocrystals (JCPDS card file no. 4-0836). Thus, the XRD patterns confirm the presence of $Cu_ySb_{2-x}(O,OH)_{6-7}$ mixed crystals and indicates the presence of Cu_2O as well as Cu nanocrystals.

Considering the main peak at $2\theta = 30.1699^\circ$, the average crystallite diameter calculated using Scherrer's formula:

$$d = 0.9\lambda/\mathrm{FWHM}\cos 2\theta \quad (\text{peak}) \tag{1}$$

where λ is the wavelength of X-ray radiation (CuKα = 1.5406 Å), FWHM is the full width at half maximum at 2θ. Table 1 (column 8) shows that the average sizes of both the Cu_2O and $Cu_ySb_{2-x}(O,OH)_{6-7}$ ($y \leq 2, x \leq 1$) nanocrystals increases from 35 nm to 70 nm (error ±1 nm) with increasing concentration of Cu from 2.0 to 3.5 wt% respectively. It must be mentioned here that repeated synthesis of the nanocomposites and their XRD analysis shows the above mentioned peaks of Cu_2O and $Cu_ySb_{2-x}(O,OH)_{6-7}$ ($y \leq 2$, $x \leq 1$) nanoparticles with variation of intensity ±1%. This manifests that the nanocrystals are formed due to the highly reactive and mild reducing property of Sb_2O_3 and is not just the result of any accidental or uncontrolled crystallization while casting or annealing.

3.3. UV–vis spectra analysis

On the contrary, optical spectroscopy is a powerful technique and any slight changes in composition (with respect to dopant concentration) of the glasses are noticeably detected. Optical absorption spectra of the undoped (B) and doped nanocomposites (NC1–NC7) are shown in Fig. 4. The undoped glass shows absence of any features (see Fig. 4, curve a) indicating that the base glass matrix is transparent in the spectral region of interest to this study. However, the absorption spectra interestingly show two types of absorption corresponding to the two types of nanocomposites. The absorption spectra of the yellow and orange colored nanocomposites (NC1–NC6) clearly depicts size-controlled band gap (E_g) shift of the semiconductor (Cu_2O) nano-crystallites embedded in the glass (see Fig. 4, curves b–g). The UV absorption edges experiences a red shift with increasing dot size from NC1 to NC6. The shift in the UV absorption edges (or fundamental absorption cut-off) with respect to the undoped base glass with increasing dopant concentration can be seen more clearly in the transmission spectra (Fig. 5) as given later.

Thereafter, there is a sudden jump in absorption in case of the red nanocomposite NC7. Its absorption spectra (Fig. 4, curve h) is completely different from the previous ones and corresponds very well to the SPR band of nano metallic Cu with the SPR maxima at 529 nm. It can therefore be proposed that under high concentrations of copper dopant in nanocomposite NC7, metallic Cu nanoparticles are produced through the deeper reduction of the oxide; however the quantity of the metal is not too large to be explicitly detected by XRD. But, the metal appears in optics due to the greater absorption efficiency of metallic Cu nanoparticles than

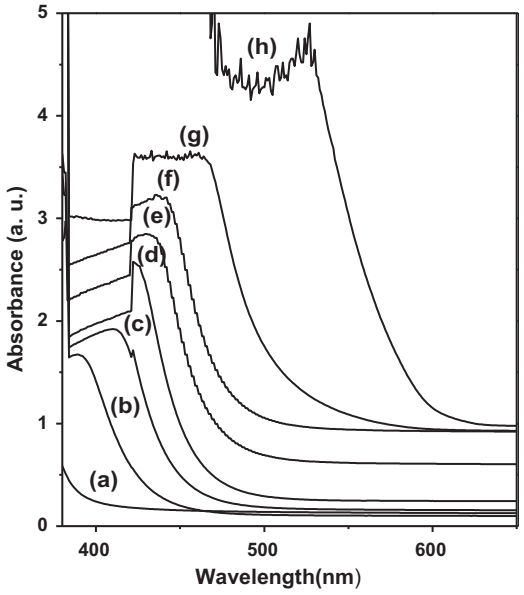

Fig. 4. UV–vis absorption spectra of nanocomposites: (a) G, (b) NC1, (c) NC2, (d) NC3, (e) NC4 (f) NC5, (g) NC6 and (h) NC7 (thickness: 1.0 mm, for composition see Table 1).

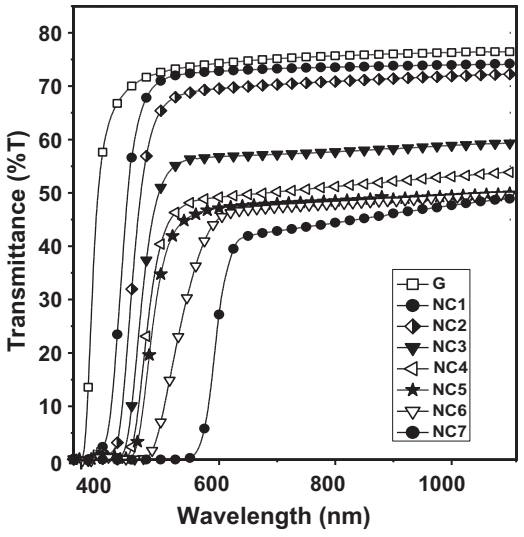

Fig. 5. UV–vis transmission spectra of base glass G and nanocomposites: NC1, NC2, NC3, NC4, NC5, NC6 and NC7 (thickness: 1.0 mm, for composition see Table 1).

semiconductor Cu_2O. It also be noted here that $Cu_ySb_{2-x}(O,OH)_{6-7}$ ($y \leq 2$, $x \leq 1$) crystals are not known to display SPR while the SPR does not appear effectively for semiconductor particles, even for the narrow band gap ones, because their free carrier concentration is rather low at room temperatures and requires high power excitation light.

The efficient optical band gap or width of the forbidden zone can be determined from the plot of $(\alpha h\upsilon)^2$ versus $h\upsilon$ following the Mott and Davis expression for direct transitions [45]:

$$\alpha(\upsilon) = \frac{B(h\upsilon - E_g)^n}{h\upsilon} \tag{2}$$

where $\alpha(\upsilon)$ is the absorption coefficient at the frequency υ, $n = 1/2$ for allowed direct transitions, B is a constant and E_g is the band gap. The intersection of the slope of the linear part of the plot $(\alpha h\upsilon)^2$ vs. $h\upsilon$ gives the values of the E_g (in eV). A plot of this type of various nanocomposites is shown in Fig. 6 and their evaluated E_g are listed

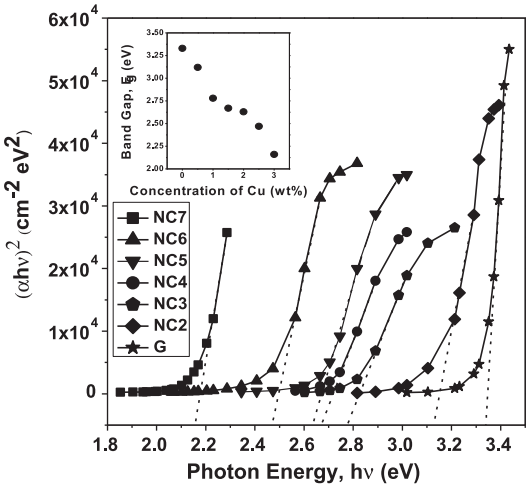

Fig. 6. $(\alpha h\upsilon)^2$ vs. $h\upsilon$ plots of base glass nanocomposite: G, NC2, NC3, NC4, NC5, NC6 and NC7. Inset shows band gap, E_g vs. concentration of Cu plot of base glass and nanocomposite: G, NC2, NC3, NC4, NC5, NC6 and NC7 (for composition see Table 1).

in Table 1 (column 6). It is seen that the E_g value decreases from 3.33 eV down to 2.16 eV with increasing concentration of Cu up to 3 wt % in the composites demonstrating quantum size effect. The Cu_2O band gap can be tuned almost the entire visible and near UV region depending upon the nanocrystalline size. This indicates their possible applications in solar cells [46]. The energy gap is the signature of size of the QDs and the bulk sample shows the lowest energy gap value. Thus, the band gap can also be tuned by controlling CuO concentration of the batch.

Thus by altering the sizes it is possible to move the transmission edge across the 350–600 nm spectral regions and this provides a way to tune the transmission edge and thereby use them as color glass filters as shown in Fig. 5. It has great technological importance and their properties are comparable to those of commercial GG, OG and RG series of sharp cut-off scattering glass filters of Schott Glass Technologies, Germany [47]. Similar shift of the UV absorption edge to the end of the visible range have observed in case of CdS, CdSe or CdTe containing striking glasses as well [1,10,48,49].

The percent transmission of the nanocomposites decreases with increase in Cu concentration. This is due to the development of incipient nanocrystalline phases which act as scattering centers. When the particles diameter are much smaller than the wavelength of visible light ($d \ll \lambda/20$), the Rayleigh scattering phenomenon takes [48–50]. The scattering loss or turbidity τ is given by [48,49]:

$$t = \frac{32\pi^4 d^3 (n\,\Delta n)^2 NV}{3\lambda^4} \quad (3)$$

where d is the particle size, λ is the wavelength of light, n is the refractive index, N is the number density of particles and V is the volume of the particles. Borrelli et al. [50] have emphasized that quantum confinement effects are not present in color filter glasses, because the crystals (such as CdS, CdSe or CdTe) present in commercial filter glasses are too large (average diameter more than 10 nm) to display strong quantum size effects. Thus, in the present investigation both QDs and larger sizes of Cu_2O particles were formed in the nanocomposites (NC1–NC7).

The transmission spectra (Fig. 5) also confirm the absence of Cu^{2+} ions because Cu^{2+} ions are known to exhibit absorption band between 600 and 800 nm due to $^2B_{1g} \rightarrow {}^2B_{2g}$ transition.

3.4. TEM and SAED images

The TEM image was taken for the monolithic nanocomposite NC7 which has the possibility of containing the maximum number of nanocrystallites. The TEM image of the nanocomposite NC7 (Fig. 7) shows the presence nanoparticles of both spherical and elliptical morphologies dispersed within the glass matrix, having a wide range of size distribution from about 5 to 42 nm (error ±1 nm). This again emphasizes that both QDs and larger sizes of nanoparticles were formed. The discrepancy between the nanocrystallite sizes estimated from the TEM image and XRD patterns is due to the fact that the TEM image represents only a particular section of the sample while the XRD patterns gives the average nanocrystallite sizes.

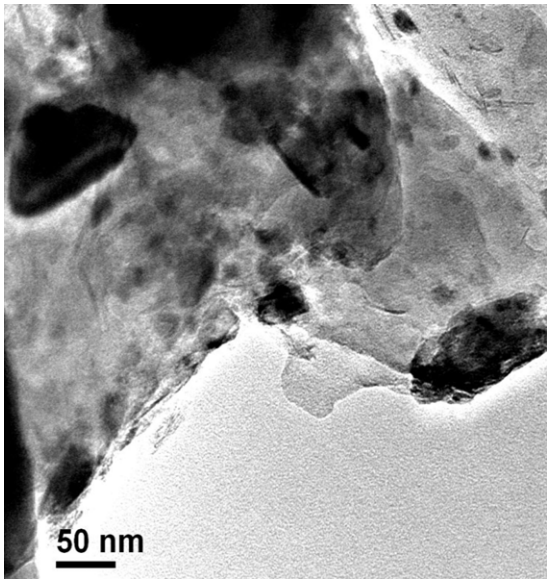

Fig. 7. TEM image of the nanocomposite NC7 (for composition see Table 1).

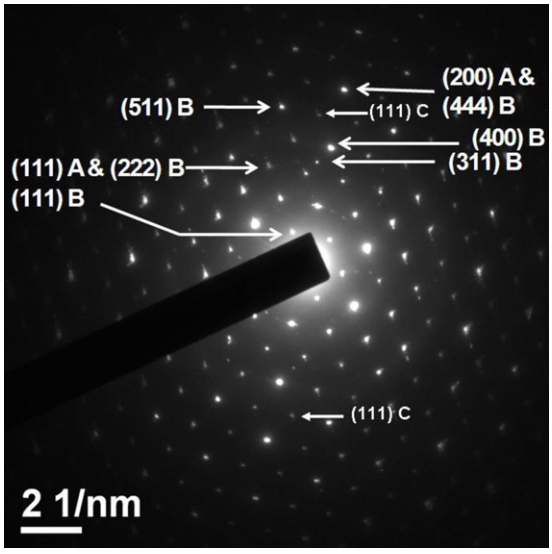

Fig. 8. SAED of an individual polycrystalline nanoparticle where A = Cu_2O, B = $Cu_ySb_{2-x}(O, OH)_{6-7}$ ($y \le 2, x \le 1$) and C = Cu.

The selected area electron diffraction (SAED) pattern (Fig. 8) confirms the formation of three types of crystals i.e. Cu_2O, $Cu_ySb_{2-x}(O,OH)_{6-7}$ ($y \le 2$, $x \le 1$) and Cu. Thus the SAED spectrum discloses the polycrystalline nature.

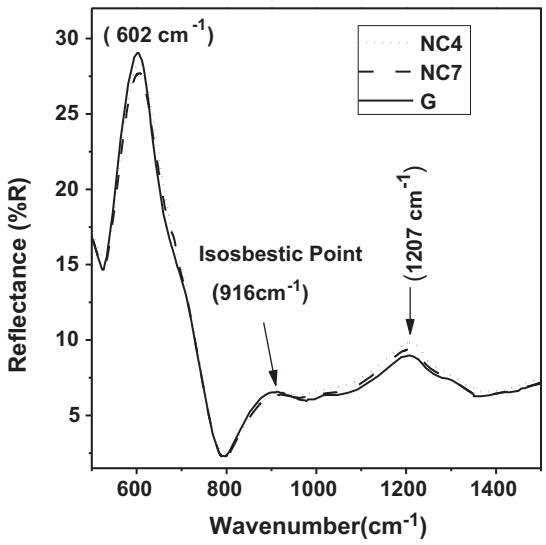

Fig. 9. Infrared reflection spectra (FT-IRRS) spectra of base glass and nanocomposite: G, NC4 and NC7 (for composition see Table 1).

3.5. Infrared reflection spectra (IRRS) analysis

IRRS spectra in the range 500–1500 cm^{-1} of undoped (NC1) glass and nanocomposites (NC5 and NC8) are shown in Fig. 9. There are two major reflection bands centered at about 602 and 1207 cm^{-1}. The band at 602 cm^{-1} is attributed to Sb–O–Sb stretching vibration [41] and that at 1207 cm^{-1} is to the stretching vibration of the B–O in [BO_3] unit [41]. The band at around 602 cm^{-1} is also related with Cu–O bond in Cu_2O [51]. It is seen that as Cu concentration increases, the 602 cm^{-1} band shifts towards higher frequency (from 602 cm^{-1} to 606 cm^{-1}) and its reflectivity (intensity) decreases (from 29% down to 27%). It is, thus, evident that there must have been some Sb–O–Cu bond formation in the nanocomposites. On the other hand, the 1207 cm^{-1} band position remains almost unshifted but its reflectivity (intensity) increases (from 9% to 11%) with increasing concentration of Cu. As a consequence of intensity increase in the band 1207 cm^{-1} and decrease in the band around 602 cm^{-1}, all the curves cross at around 916 cm^{-1}. This crossing point is known as isosbestic point which represents the existence of equilibrium between the molar reflectivity of both species of Sb–O and B–O bonds.

The shifting of the 602 cm^{-1} band position can be illustrated by the Szigeti relation of fundamental vibration frequency, υ (in cm^{-1}) as follows [52]:

$$\upsilon = \left(\frac{k}{4\pi^2 c^2 \mu}\right)^{0.5} \quad (4)$$

which stipulates that the position of IR bands, and is related to the force constant (k), reduced mass (μ) and speed of light (c). The μ, in this case, can be defined by

$$m = {m_1}^{-1} + {m_2}^{-1} + {m_3}^{-1} \quad (5)$$

where m_1, m_2 and m_3 are the masses of the bond forming two atoms. It is, therefore, obvious from the above two equations that frequency (υ) at 602 cm^{-1} increases with decreasing μ due to the incorporation of lighter Cu into the antimony phase due to chemical interaction between CuO and Sb_2O_3. There is no shift in the band position of the borate species at 1207 cm^{-1} indicating that the Cu did not enter into borate phase. The shift in band position is a strong evidence in favor of Sb–O–Cu bond formation and thereby the formation $Cu_ySb_{2-x}(O,OH)_{6-7}$ ($y \le 2, x \le 1$) crystals.

It is well known that the intensity of an IR band is directly controlled by the dipole moment (μ_{DM}) gradient, $\delta\mu_{DM}$ and indirectly by the force constant (k). The k (in mdyn $Å^{-1}$) may be expressed as [53]:

$$k = 1.67N\left(\frac{\chi_1\chi_2}{r^2}\right)0.75 + 0.3 \quad (6)$$

where N is the bond order, χ_1 and χ_2 are the electronegativities of the atoms, and r is the bond distance. The changes in μ_{DM}, r, k, etc., which have happened due to the incorporation of Cu_2O and $Cu_ySb_{2-x}(O,OH)_{6-7}$ ($y \le 2, x \le 1$) crystallites in the glass matrix, are thus responsible for the decrease and increase in intensity of the bands at 602 and 1207 cm^{-1}, respectively. As a consequence of this fact, the IRRS curves show an isosbestic point at 916 cm^{-1} manifesting an existence of equilibrium between the existing species. The observation of isosbestic point at 916 cm^{-1} is a good evidence of presence of antimony and borate as the two principal species. It is also a strong argument in favor of the existence of equilibrium between them in presence of Cu_2O and $Cu_ySb_{2-x}(O,OH)_{6-7}$ ($y \le 2$, $x \le 1$) crystals.

All the other nanocomposites also exhibit similar IRRS spectra but due to clear visibility of the isosbestic point and other spectral features only two nanocomposites NC4 and NC7 having lower and higher concentration of Cu respectively is represented along with the base glass.

3.6. Infrared transmission spectra (FT-IRTS) analysis

The IR transmission (FT-IRTS) spectra, particularly in the fingerprint region, provide much information about structure (short range order) consequently the powdered nanocomposites were studied following the KBr pellet method and compared with those of base glass and raw materials.

Fig. 10, curve a shows the FT-IRTS spectrum of reagent CuO. The broad peak at 508 cm^{-1} is attributed to Cu(II)–O stretching vibration modes [51]. Fig. 10, curve b displays the FT-IRTS spectra of reagent $KBO_2{\cdot}xH_2O$. Its IR spectrum can be divided into three major (active) regions. The first group of bands lies between 1200 and 1500 cm^{-1} is attributed as the asymmetric stretching vibration of the B–O–B bond of trigonal [BO_3] units. The second group of bands which occur 800–1200 cm^{-1} is due to asymmetric stretching vibration of the B–O–B bond of tetragonal [BO_4] units. The third group around 646 and 708 cm^{-1} is due to bending vibration of B–O–B linkages in the borate network [54]. The very strong and broad hydroxyl absorption band around 3462 cm^{-1} indicates the presence of water due to water present(15.7 wt% H_2O) in the reagent ($KBO_2{\cdot}xH_2O$).

Fig. 10, curve c depicts the FT-IRTS spectrum of raw material Sb_2O_3 powder used in glass preparation. The sharp peak at 739 cm^{-1} corresponds to the symmetric stretching vibration mode of senarmontite form of SbO_3 trigonal pyramids having C_{3V} symmetry [42]. The small peak at 954 cm^{-1} is also recognized as the Sb–O stretching vibrations of senarmontite form of SbO_3 [41]. The bands located at 692, 592, 546 and 492 cm^{-1} correspond to symmetric stretching, asymmetric stretching, symmetric bending and asymmetric bending vibration modes of valentinite form of SbO_3 trigonal pyramids with C_s or C_2 symmetry, respectively [41,42].

Within the antimony base glass (Fig. 10, curve d) the main peak at 592 cm^{-1} and the small peak at 685 cm^{-1} are recognized as the Sb–O–Sb asymmetric and symmetric stretching vibrations respectively emphasizing the closeness of glass structure with valentinite Sb_2O_3 [41,42]. In addition, the region between 1000–1200 and 1200–1500 depict the asymmetric stretching vibration of the B–O–B bond of tetragonal [BO_4] and trigonal [BO_3] units respectively. The peak at 1231 cm^{-1} is probably arises due to B–O stretching vibrations of $(BO_3)^{3-}$ unit in metaborate chains [54]. The small peak at 931 cm^{-1} probably arises due to Sb–O stretch-

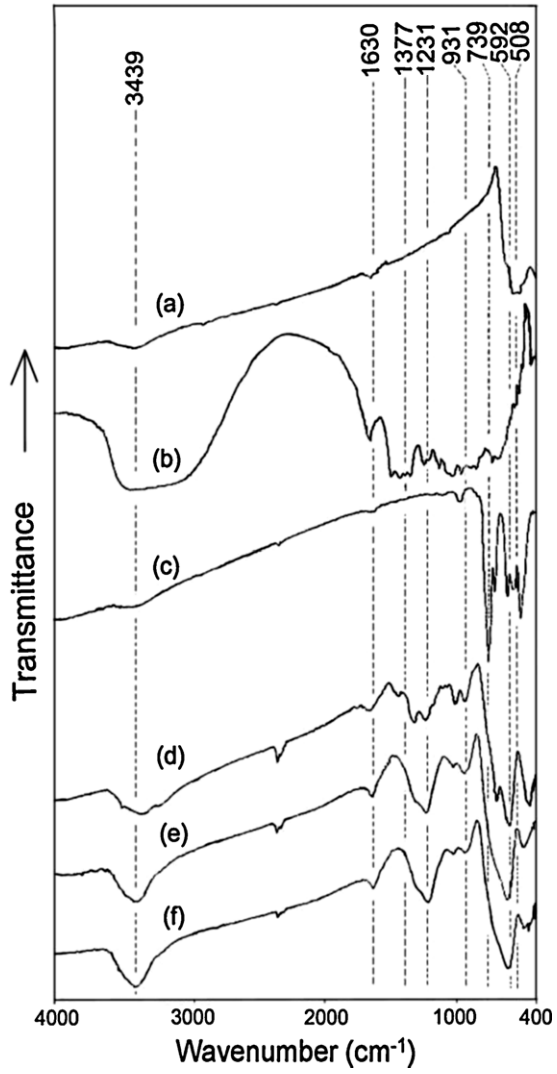

Fig. 10. Infrared transmission spectrum (FT-IRTS) of raw materials, base glass and nanocomposite taken by the KBr pellet method: (a) CuO, (b) $KBO_2 \cdot xH_2O$, (c) Sb_2O_3, (d) G, (e) NC4 and (f) NC8 (for composition see Table 1).

ing vibrations of the senarmontite form present in minor amount within the antimony glasses. This 931 cm^{-1} peak position also coincides with Si–O stretching vibration of SiO_4 tetrahedra, which were contaminated from the silica crucible during the melting process. This is supported by the EDX spectrum of the base glass (Fig. 2). The peak at 1630 cm^{-1} is endorsed as bending vibrations of O-H group of H_2O molecules while the broad band at 3439 cm^{-1} corresponds to the asymmetric stretching of O–H bond of the glass network. [55].

The peak at 592 cm^{-1} can also be attributed to Cu(I)–O stretching vibration [51]. Thus, with addition of CuO, nanocomposites NC4 and NC8 (curves e and f, respectively) the small peak at 685 cm^{-1} vanishes and merges with the 592 cm^{-1} peak which broadens in turn. The peak at 508 cm^{-1} of CuO is also absent. This indicates the absence of CuO in Cu doped nanocomposites. Hence the formation of Cu–O–Sb bond by Cu_2O is suggested. The small peaks due to metaborate linkages merge and the shape of borate peaks also changes suggesting strong chemical interaction between Cu and B related species. The broad peak at 3439 cm^{-1} suggests the presence of hydroxyl groups in the composites. These have been more clearly stated in Table 2. Thus, the FTIR-TS spectra clearly support the formation of $Cu_ySb_{2-x}(O,OH)_{6-7}$ ($y \leq 2, x \leq 1$) as well. It is interesting to note that the band due to free hydroxyl group at

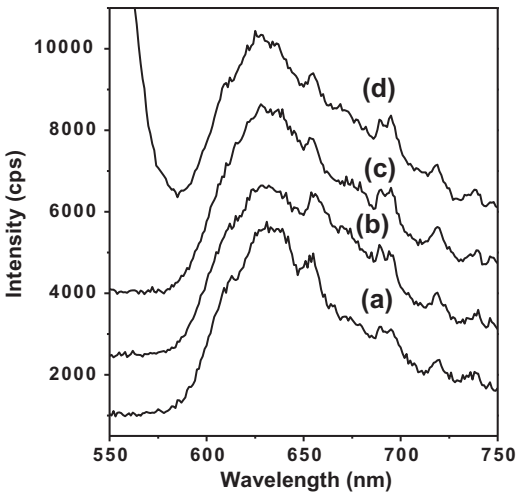

Fig. 11. Photoluminescence emission spectra of nanocomposite NC7 excited (λ_{ex}) at (a) 210 nm, (b) 230 nm, (c) 250 nm and (d) 270 nm (for composition see Table 1).

3554 cm^{-1} and hydrogen bonded hydroxyl group at 3277 cm^{-1} in the base glass, have disappeared in the nanocomposites NC4 and NC8. It is, therefore, quite reasonable to suggest that the Cu bonded with the glass matrix mainly through these linkages. This again supports the formation of $Cu_ySb_{2-x}(O,OH)_{6-7}$ ($y \leq 2, x \leq 1$) crystalline phases in nanocomposites.

All the other nanocomposites also exhibit similar FT-IRTS. For clear depiction of the spectral features only two nanocomposites NC4 and NC8 (curves e and f) having lower and higher concentration of Cu respectively is represented excluding the others.

3.7. Photoluminescence spectra analysis

Photoluminescence (PL) emission measurement was carried out with excitation wavelengths varying from 210 to 270 nm of composite NC7 (Fig. 11). It displays a broad and strong red emission band peaked at 626 nm along with small peaks at around 650, 690 and 710 nm for the entire excitation range 210–270 nm. The emissions from the other nanocomposites (NC1–NC6) are not so prominent upon excitation with similar UV light.

Earlier in 1969, Mooradian had observed fluorescence from bulk copper metal with an emission maximum at 600 nm and very low quantum yield [56]. Darugar et al. [30] observed much stronger fluorescence from Cu nanoparticles at 610 nm upon lower UV wavelength excitation. They explained the phenomenon as radiative recombination of the s–p conduction-band electrons below the Fermi level with the holes in the d-bands. The fluorescence of Cu nanocrystals are stronger than bulk copper metal possibly due to localized surface plasmon resonance induced enhancements of the electric fields of the incoming and out-going radiation [30]. Luminescence in the same red wavelength region has also been observed for nanocrystalline Cu_2O. Cu_2O exhibits emission peaks between 600 and 640 nm due to phonon assisted transitions [27].

It is therefore suggested that the broad red emission peak with the main maximum at 626 nm along with a sharp peak around 650 nm is probably due to the overlap of the emission due to Cu nanocrystals and the transitions between $^3\Gamma_5^+$ valence band and $^2\Gamma_7^+$ conduction band in Cu_2O nanocrystals [27]. The shape, position and intensity of the emission band has changed negligibly with the change in excitation wavelength indicating that it is a genuine luminescence peak arising from the radiative transitions between the quantum energy levels solely attributed due to Cu_2O and Cu nanoclusters present in the composite. The absence of similar emission peaks in the base glass manifests this statement. The

Table 2
FT-IRTS band position in raw materials, glass and nanocomposites along with band assignment.

Sample identity/band positions (± 2, cm^{-1})						Band assignments
CuO	$KBO_2{\cdot}xH_2O$	Sb_2O_3	G[a]	NC4[a]	NC8[a]	
			3554(w)			Free hydroxyl group O–H (s-s)
3453(w,b)	3462(s,b)	3508(w)	3392(s,b)	3446 (s,b)	3439(s,b)	O–H (s-v)
			3277(w)			Hydrogen bonded (–O–$H^{\delta+}\cdots O^{\delta-}$–) (s-v)
	1646(m)	1615(w)	1654(m,b)	1631(m)	1631(m)	H–O–H (b-v)
	1377(w)		1431(w)			B–O–B in [BO_3] (as-s)
			1315(m)	1315(sh)		B–O–B in [BO_3] (as-s)
	1231(w)		1231(m)	1231(m,b)	1231(m)	B–O in $(BO_3)^{3-}$ (as-v)
	1008(w)		1000(m)	1015(w)	1023(m)	B–O–B in [BO_4] (as-s)
		954(m)	931(m)	931(m)	931(m)	O–Sb–O (s-v) (senarmontite) O–Si–O (s-v)
		739(s)				O–Sb–O (s-s) (senarmontite)
		692(m)	685(m)			O–Sb–O (s-s) (valentinite)
		592(m)	592(s)	604(s)	608(s)	O–Sb–O (as-s), (valentinite) O–Cu(I)–O (s-s)
		546(m)				O–Sb–O (s-b), (valentinite)
508(s,b)						O–Cu(II)–O (s-v)
		492(s)	438(s)	477(m)	438(w), 492(w)	O–Sb–O (as-b) (valentinite)

s = strong, b = broad, w = weak, sh = shoulder, m = medium, s-s = symmetric stretching vibration, as-s = asymmetric stretching vibration, s-b = symmetric bending vibration, as-b = asymmetric bending vibration, s-v = stretching vibration, b-v = bending vibration.
[a] For composition see Table 1.

small sharp peak at around 690 nm is probably due to transitions between $^3\Gamma_5^+$ valence band and $^2\Gamma_3^+$ conduction band in Cu_2O nanocrystals while the peak around 710 nm is probably due to any lattice imperfections or other recombination of carriers through donors/acceptors [27–29].

Sb_2O_3 is 10 and 100 times less poisonous than lead and cadmium oxides respectively [57]. The permissible limit (of occupational safely and health administration) of Sb_2O_3 in humans is 0.5 mg/m^3, which is 50 times more than arsenic [57]. However, since the main route of exposure is by inhalation of the dust, hence care should be taken during batch preparation [57].

4. Conclusions

We have demonstrated here a new and very simple single-step methodology (thermochemical reduction) to prepare cuprous oxide (Cu_2O) antimony glass (K_2O–B_2O_3–Sb_2O_3) nanocomposites without addition of any external reducing agent. At the same time $Cu_ySb_{2-x}(O,OH)_{6-7}$ ($y \leq 2$, $x \leq 1$) and Cu crystalline phases are also produced. Their formations are confirmed by XRD analysis. Polycrystalline character of produced nanoparticles is established by SAED analysis. The average nanocrystallite sizes were calculated using Scherrer's formula is found to vary in the range 35–70 nm. It is supported by TEM image as well. EDX spectrum confirmed existence of Cu in the nanocomposites. Formation of two types of nanocomposites is exemplified by the UV–vis spectra. The UV–vis spectra of the yellow and orange colored nanocomposites show size-controlled band gap shift of the semiconductor (Cu_2O) nanocrystallites embedded in the glass from 3.33 eV down to 2.16 eV while the red nanocomposite exhibits surface plasmon resonance band at 529 nm due to formation of metallic Cu at higher concentration. The transmission spectra of these nanocomposites show distinct red shift of the absorption edges. Their properties are comparable to those of commercial GG, OG and RG series of sharp-cut scattering glass filters of Schott Glass Technologies, Germany. The red nanocomposite when excited in the range 210–270 nm shows strong broad red emission peak with the main maximum at 626 nm along with several sharp peaks probably due to the overlap of the emission due to Cu nanocrystals and the transitions the valence and conduction levels in Cu_2O nanocrystal. We are the first to report the single-step synthesis of monolithic ruby red cuprous oxide antimony glass nanocomposites. This methodology may also pave the pathway for the production of bulk industrial ruby red glasses having uniform bright coloration at nominal expenditure.

Acknowledgements

One of the authors (TS) gratefully acknowledges the financial support of the Council of Scientific and Industrial Research (CSIR), New Delhi in the form of NET-SRF under sanction number 31/015(0060)/2007-EMR-1. They gratefully thank the director of the institute for his kind permission to publish this work. The technical supports provided by the infrastructural facility (X-ray Division) of this institute and the National Facility Center, IIT Kharagpur (TEM Division) are also thankfully acknowledged.

References

[1] W.A. Weyl, Colored Glasses, The Society of Glass Technology, Sheffield, Great Britain, 1951, p. 420.
[2] W. Vogel, Glass Chemistry, Springer-Verlag, Berlin, 1992.
[3] J. Lafait, S. Berthier, C. Andraud, V. Reillon, J. Boulenguez, Comp. Ren. Phys. 10 (2009) 649–659.
[4] V.S. Gurina, A.A. Alexeenkob, K.V. Yumashevc, P.V. Prokoshinc, S.A. Zolotovskayac, G.A. Zhavnerko, Mater. Sci. Eng. C 23 (2003) 1063–1067.
[5] I. Nakai, C. Numako, H. Hosono, K. Yamasaki, J. Am. Ceram. Soc. 82 (1999) 689–695.
[6] M.O. Figueriedo, J.P. Viega, J.P. MirÃo, Appl. Phys. A 83 (2006) 499–502.
[7] R. Arletti, M.C. Dalconi, S. Quartieri, M. Triscari, G. Vezzalini, Appl. Phys. A 83 (2006) 239–245.
[8] F. Farges, M.-P. Etcheverry, A. Scheidegger, D. Grolimund, Appl. Geochem. 21 (2006) 1715–1731.
[9] A. Ruivo, C. Gomes, A. Lima, M.L. Botelho, R. Melo, A. Belchior, A.P. de Matos, J. Cult. Herit. 9 (2008) e134–e137.
[10] J.A. Williams, G.E. Rindone, H.A. McKinstry, J. Am. Ceram. Soc. 64 (1981) 702–709.
[11] S. Banerjee, A. Paul, J. Am. Ceram. Soc. 57 (1974) 286–290.
[12] R.S. Singh, S.P. Singh, J. Mater. Sci. 38 (2003) 1551–1557.
[13] S. Rada, A. Dehelean, E. Culea, J. Alloys Compd. 509 (2011) 321–325.
[14] M.V.N. Padma Rao, V. Ravikumar, L.S. Rao, P.V. Rao, M.S. Reddy, N. Veeraiah, J. Alloys Compd. 472 (2009) 489–496.
[15] N. Srinivasa Rao, L. Srinivasa Rao, Y. Gandhi, V. Ravikumar, N. Veeraiah, Physica B 405 (2010) 4092–4100.
[16] L.S. Rao, M.S. Reddy, D.K. Rao, N. Veeraiah, Solid State Sci. 11 (2009) 578–587.
[17] A. Quaranta, R. Ceccato, C. Menato, L. Pederiva, N. Capra, R.D. Maschio, J. Non-Cryst. Solids 345–346 (2004) 671–675.
[18] H.D. Schreiber, M.A. Stone, A.M. Swink, J. Non-Cryst. Solids 352 (2006) 534–538.
[19] T. Bring, B. Jonson, L. Kloo, J. Rosdahl, Glass Technol.-Eur. J. Glass Sci. Technol. Part A 48 (2007) 142–148.
[20] S.F. Brown, F.H. Norton, J. Am. Ceram. Soc. 42 (1959) 499–503.
[21] R. Doremus, S.-C. Kao, R. Garcia, Appl. Opt. 31 (1992) 5773.
[22] A. Ram, S.N. Prasad, Mechanism of formation of color in copper red glass, in: Advances in Glass Technology, Part I, Plenum Press, New York, 1962, pp. 256–269.
[23] M. Wakamatsu, N. Takeuchi, S. Ishida, J. Non-Cryst. Solids 80 (1986) 412–421.
[24] D.P. Dubal, D.S. Dhawale, R.R. Salunkhe, V.S. Jamdade, C.D. Lokhande, J. Alloys Compd. 492 (2010) 26–30.
[25] N. Brun, L. Mazerolles, M. Pernot, J. Mater. Sci. Lett. 10 (1991) 1418–1420.

[26] M. Gracinda Ferreira da Silva, J.M. Fernandez Navarro, J. Non-Cryst. Solids 100 (1988) 447–452.
[27] M.I. Freedhoff, A.P. Marchetti, Quantum confinement in semiconductor nanocrystals, in: R.E. Hummel, P. Wíssman (Eds.), Handbook of Optical Properties, vol. 2, CRC Press, Boca Raton, 1997.
[28] A. Sengupta, J.Z. Zhang, Semiconductor nanoparticles, in: Z. Lin Wang, Y. Liu, Z. Zhang (Eds.), Handbook of Nanophase and Nanostructured Materials, vol. 3, Plenum Publishers, New York, 2003.
[29] Y. Liu, Excitons at high density in cuprous oxide and coupled quantum wells, Ph.D. thesis, University of Pittsburgh, 2004.
[30] Q. Darugar, W. Qian, M.A. El-Sayed, M.-P. Pileni, J. Phys. Chem. B 110 (2006) 143–149.
[31] A. Tang, Y. Xiao, J. Ouyang, S. Nie, J. Alloys Compd 457 (2008) 447–451.
[32] M. Valodkar, A. Pal, S. Thakore, J. Alloys Compd 509 (2011) 523–528.
[33] C. Silva, J.M.P. Coelho, A. Ruivo, A.P. de Matos, Mater. Lett. 64 (2010) 705–707.
[34] T. Lutz, C. Estournès, J.C. Merle, J.L. Guille, J. Alloys Compd. 262–263 (1997) 438–442.
[35] G. De, M. Epifani, A. Licciulli, J. Non-Cryst. Solids 201 (1996) 250–255.
[36] C. Gil, M.A. Villegas, Mater. Chem. Phys. 88 (2004) 185–191.
[37] C. Gil, M.A. Villegas, J.M. Fernández Navarro, J. Euro. Ceram. Soc. 25 (2005) 711–718.
[38] C. Capatina, Ceramics-Silikaty 49 (2005) 283–286.
[39] H. Amekura, O.A. Plaksin, K. Kono, Y. Takeda, N. Kishimoto, J. Phys. D: Appl. Phys. (2006) 3659–3664.
[40] T. Akai, K. Kadono, H. Yamanaka, T. Sakaguchi, M. Miya, H. Wakabayashi, J. Ceram. Soc. Jpn. 101 (1993) 105–107.
[41] T. Som, B. Karmakar, J. Non-Cryst. Solids 356 (2010) 987–999.
[42] D. Holland, A.C. Hannon, M.E. Smith, C.E. Johnson, M.F. Thomas, A.M. Beesley, Solid State Nucl. Magnet. Res. 26 (2004) 172–179.
[43] Y. Wang, N. Herron, J. Phys. Chem. 95 (1991) 525–532.
[44] A.A. Ahmed, G.M. Ashour, Glass Technol. 22 (1981) 24–33.
[45] N.F. Mott, E.A. Davis, Electronic Processes in Non-Crystalline Materials, 2nd edition, Clarendon Press, Oxford, 1979.
[46] A.O. Musa, T. Akomolafe, M.J. Carter, Solar Energy Mater. Solar Cells 51 (1998) 305–316.
[47] Schott Glass Technologies, Inc., Color Filter Glass, Duryea, PA, 1982.
[48] S. Musikant, Optical Materials, Marcel Dekker, New York, 1985.
[49] G. Fuxi, Optical and Spectroscopic Properties of Glass, Springer-Verlag, Berlin, 1992.
[50] N.F. Borrelli, D.W. Hall, H.J. Holland, D.W. Smith, J. Appl. Phys. 61 (1987) 5399–5409.
[51] B. Balamurugan, B.R. Mehta, Thin Solid Films 396 (2001) 90–96.
[52] B. Szigeti, Proc. Soc. London Ser. A 204 (1950) 51–62.
[53] B. Karmakar, P. Kundu, R.N. Dwivedi, J. Am. Cream. Soc. 83 (2000) 1305–1307.
[54] S.G. Motke, S.P. Yawale, S.S. Yawale, Bull. Mater. Sci. 25 (2005) 75–78.
[55] K.M. Davis, M. Tomozawa, J. Non-Cryst. Solids 201 (1996) 177–198.
[56] A. Mooradian, Phys. Rev. Lett. 22 (1969) 185–187.
[57] C.L. Yaws, Chemical Properties Handbook, McGraw-Hill, New York, 1999, p. 115 and pp. 613–615.